Supplementary Materials

Athermal glass work at the nanoscale: Engineered electron-beam-induced viscoplasticity for mechanical shaping of brittle amorphous silica

Sung-Gyu Kang [a], Kyeongjae Jeong [a], Jeongin Paeng [a], Wonseok Jeong [b], Seungwu Han [a], Jae-Pyeong Ahn [c], Steven Boles [d], and Heung Nam Han [a]*, In-Suk Choi [a]*

[a] Department of Materials Science and Engineering & Research Institute of Advanced Materials, Seoul National University, Seoul, Republic of Korea

[b] Lawrence Livermore National Laboratory, Livermore, USA

[c] Advanced Analysis Center, Korea Institute of Science and Technology, Seoul, Republic of Korea

[d] Department of Energy and Process Engineering, NTNU – Norwegian University of Science and Technology, Trondheim, Norway

* Corresponding author: Prof. Heung Nam Han and Prof. In-Suk Choi

E-mail: hnhan@snu.ac.kr and insukchoi@snu.ac.kr

Supplementary Figures

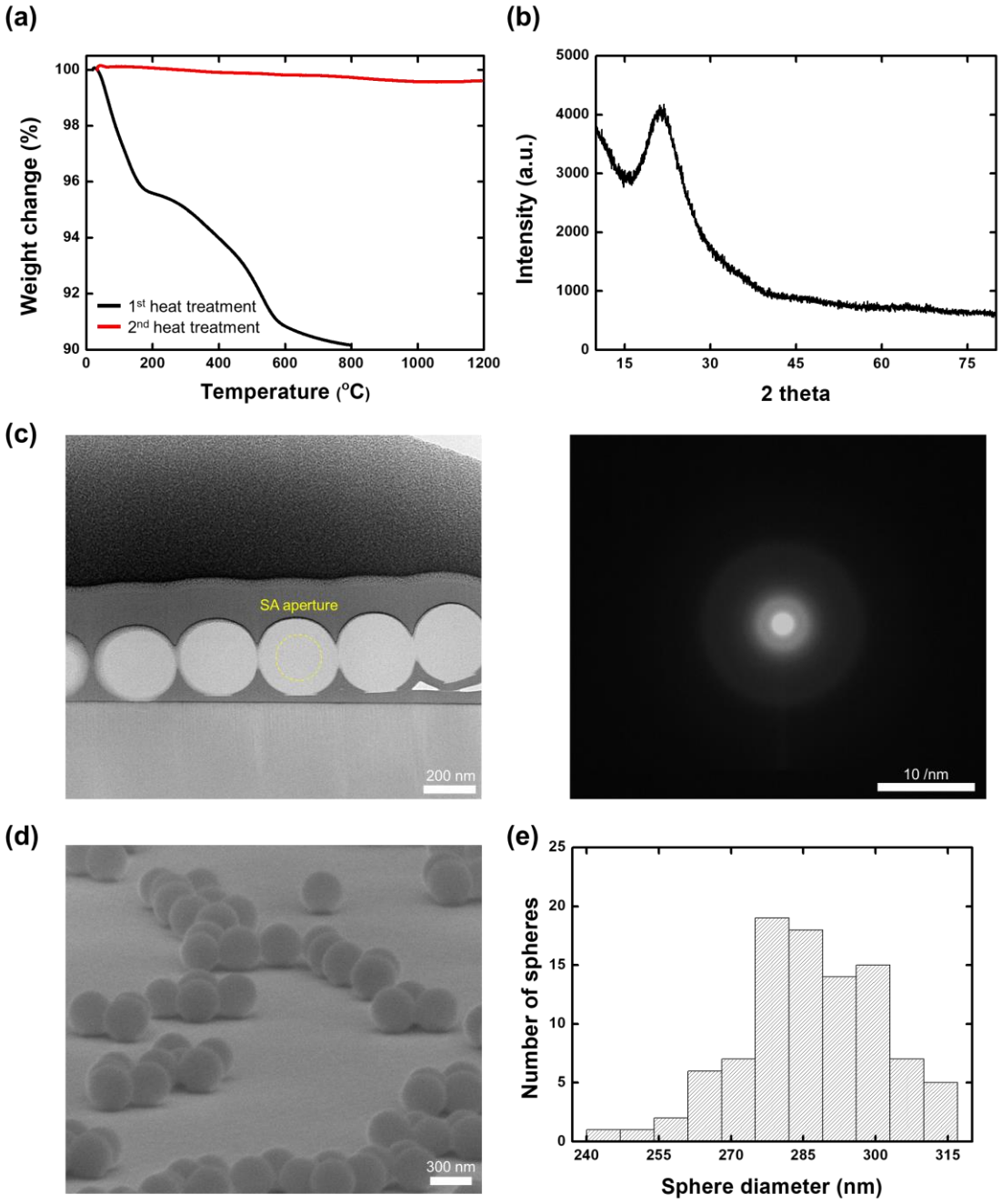

Fig. S1. Characterizations of amorphous silica spheres. (a) Thermogravimetric analysis of the as-fabricated amorphous silica spheres during the first (black curve) and second (red curve) thermal treatments at 900 ºC for 6 h. Most of the residues are removed during the first thermal treatment. (b) X-ray diffraction pattern of the amorphous silica spheres after heating. The amorphous silica spheres maintain their amorphous characters even after heating. (c) Cross-sectional TEM analysis of amorphous silica spheres after heating. Bright field image (left) and

selected area diffraction pattern (right) obtained from amorphous silica sphere denoted by yellow dashed circle. A diffuse ring pattern means that the phase of silica after the heating is amorphous. (d) Tilted scanning electron microscopy (SEM) image of the amorphous silica spheres on the sapphire substrate. (e) Diameter distribution of the amorphous silica spheres determined using 100 randomly selected spheres.

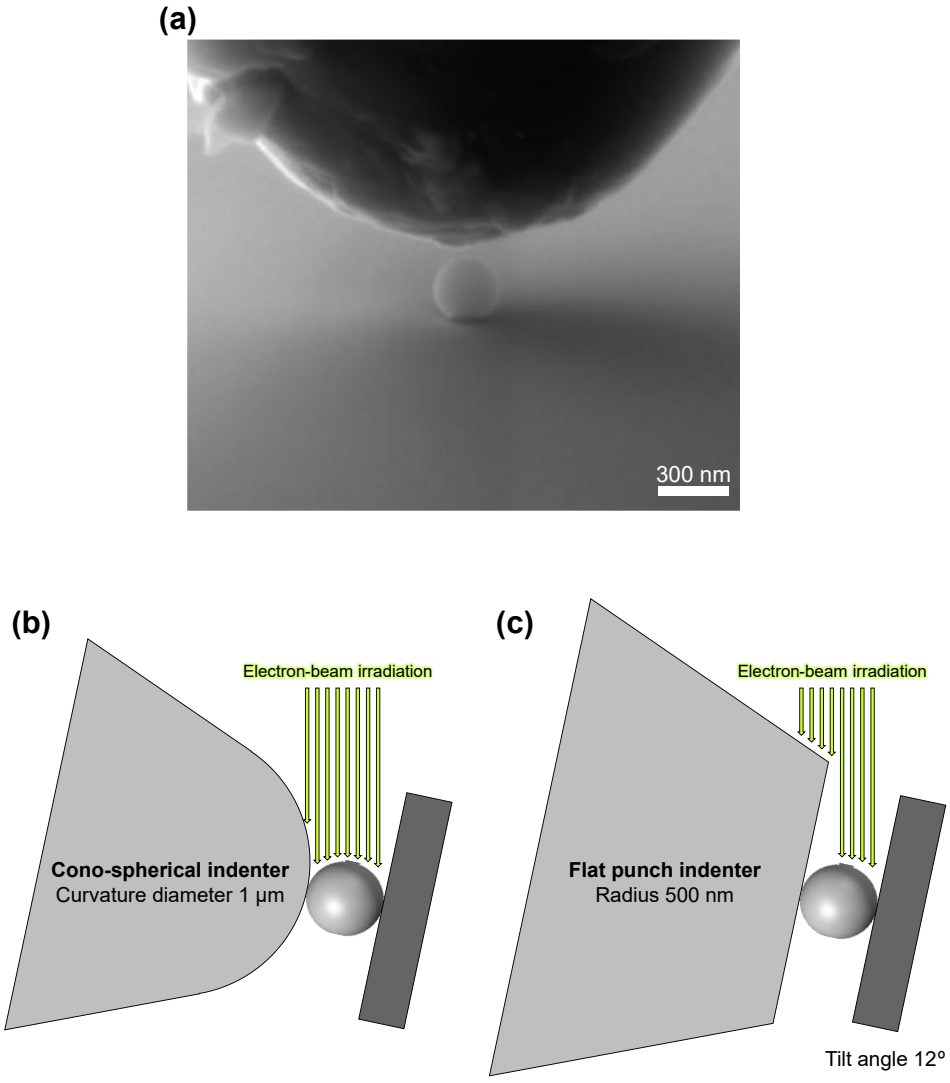

Fig. S2. Experimental set up of the *in-situ* compression test of an amorphous silica sphere. (a) Tilted SEM image of the amorphous silica sphere beneath the cono-spherical indenter prior to the compression test. Schematics of the electron-beam (e-beam) irradiation profile during the *in-situ* compression test using the cono-spherical (b) or flat punch (c) indenter.

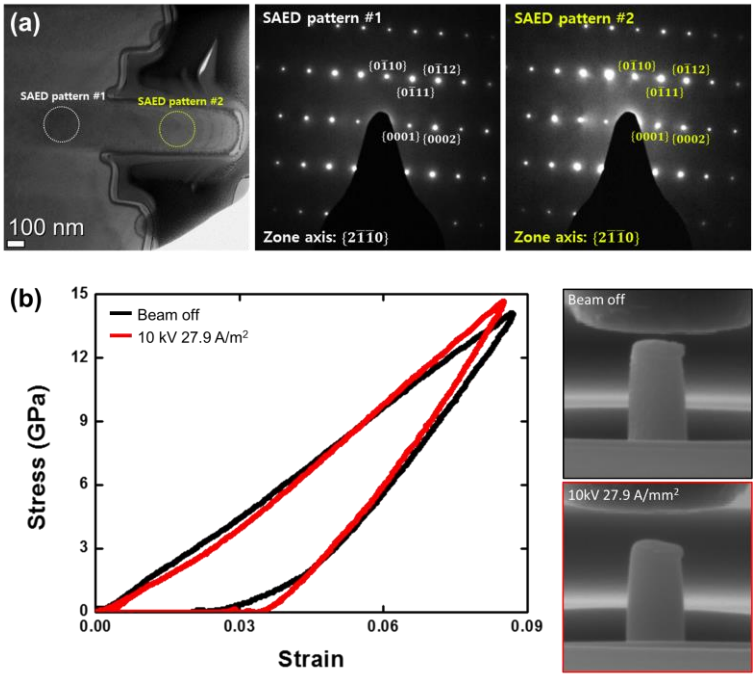

Fig. S3. in-situ compression test of single crystalline sapphire micropillar under e-beam irradiation. (a) Cross-sectional TEM analysis of micropillar (left) Dark-field TEM image of micropillar (center and right) Diffraction pattern of substrate and micropillar (b) Engineering stress-strain curves of micropillar with and without e-beam irradiation and corresponding deformed SEM images.

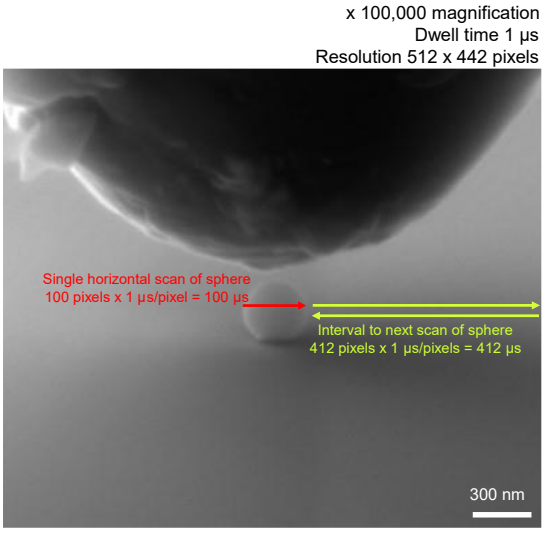

Fig. S4. Time scale of the raster SEM e-beam used in Monte Carlo simulation. Horizontal scans across the amorphous silica sphere and the sapphire substrate are indicated in red and yellow, respectively.

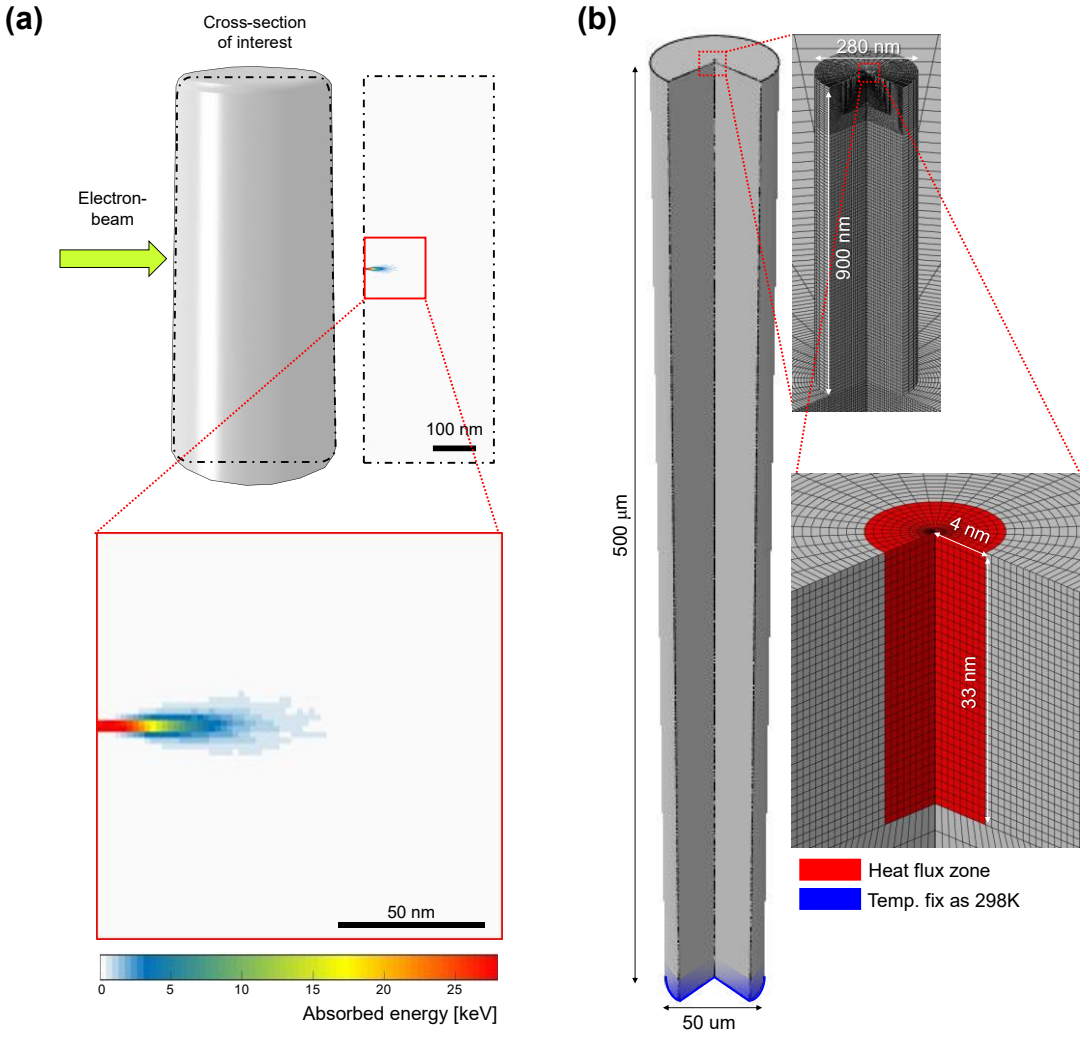

Fig. S5. Computational model of the temperature change within a fused quartz pillar under a 5 kV, 1.4 A/m^2 e-beam. (a) Absorbed energy distribution within the fused quartz pillar calculated via Monte Carlo simulation. (b) Simplified heat transfer model (ABAQUS/Standard (Ver 6.10)) of the fused quartz pillar during e-beam irradiation.

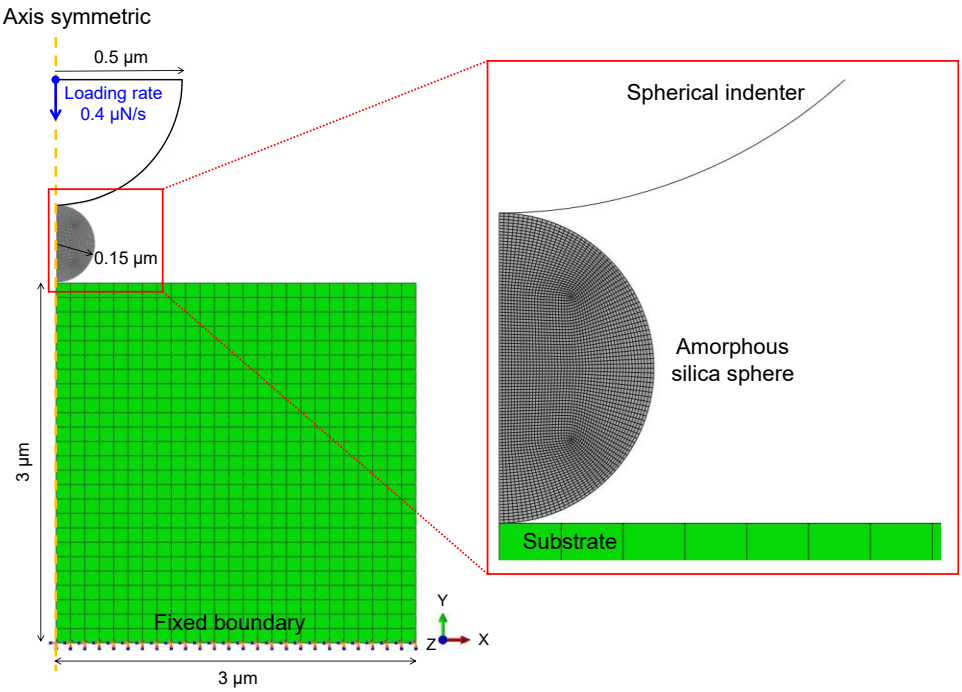

Fig. S6. Finite element method (FEM) model of the compression test of an amorphous silica sphere. The yellow dashed line represents the symmetric y-axis. The boundary condition is marked on the bottom surface of the substrate, and the load is applied to the center reference point (blue dot) of the indenter.

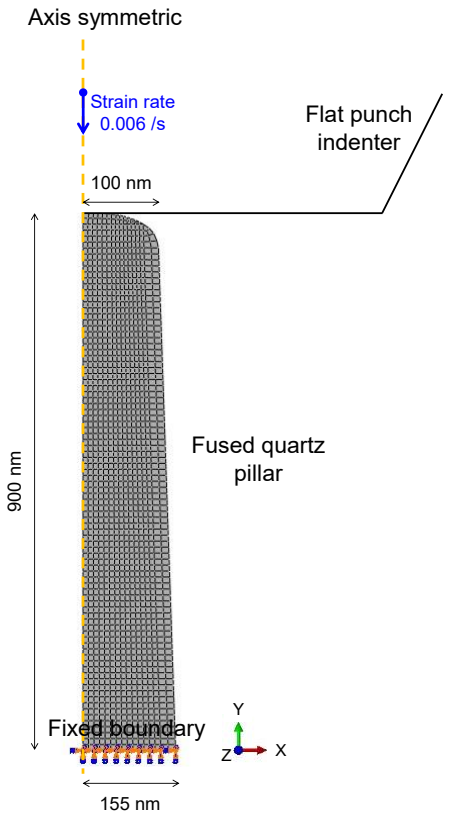

Fig. S7. FEM model of the compression test of a fused quartz pillar. The radius, height, and taper angle of the pillar are 140 and 900 nm and 2.4°, respectively. The pillar had the same mechanical properties as those of the amorphous silica sphere, and the flat punch indenter was assumed to be a rigid body. The mesh type (CAX4R), contact condition between the indenter and pillar, and the boundary condition applied to the bottom face of the pillar are the same as those used in Fig. S5. A vertical displacement in the y-direction was applied to the indenter with a strain rate of 0.006 s^{-1} until the maximum depth of 136 nm was reached.

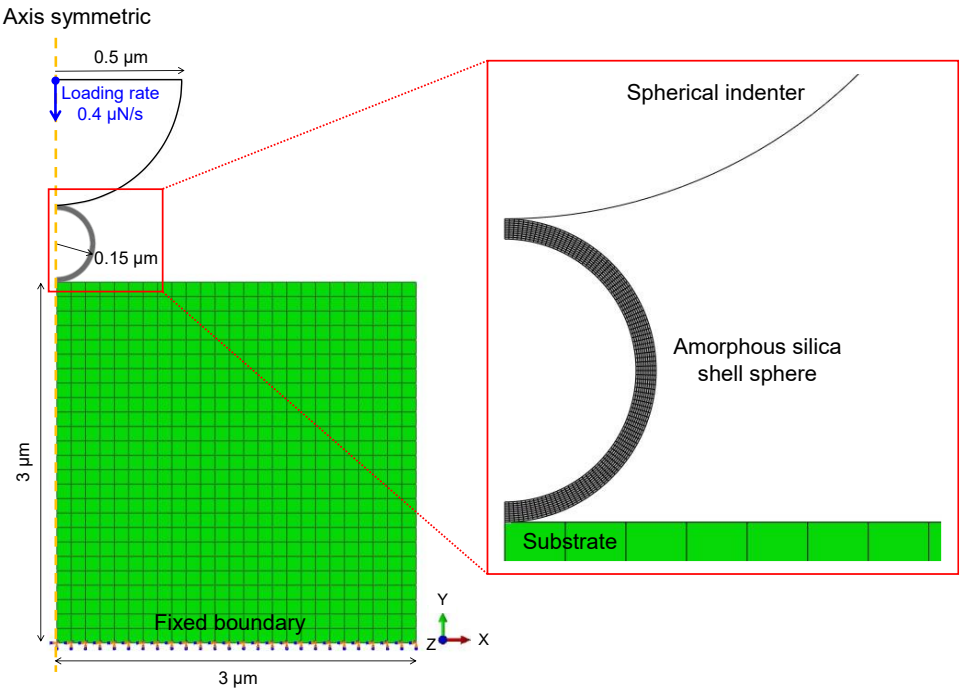

Fig. S8. FEM model for the compression test of a spherical amorphous silica nanoshell. The yellow dashed line represents the symmetric y-axis. The boundary condition is marked on the bottom surface of the substrate, and the load is applied to the center reference point (blue dot) of the indenter.

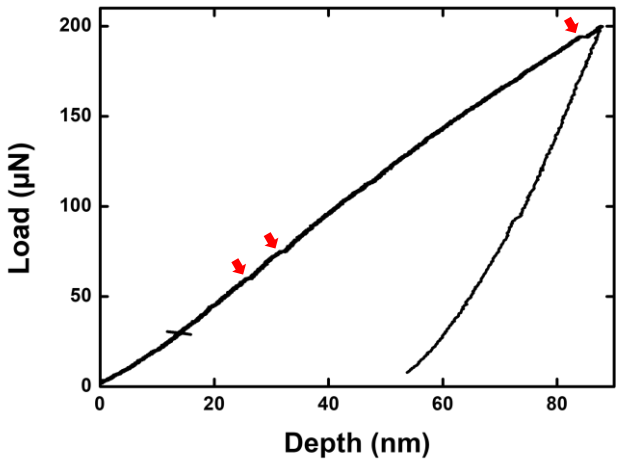

Fig. S9. Compression load-depth curve of the amorphous silica sphere up to a maximum compression load of 200 μN in the absence of electron-beam irradiation. Red arrows indicate crack formation associated pop-in events.

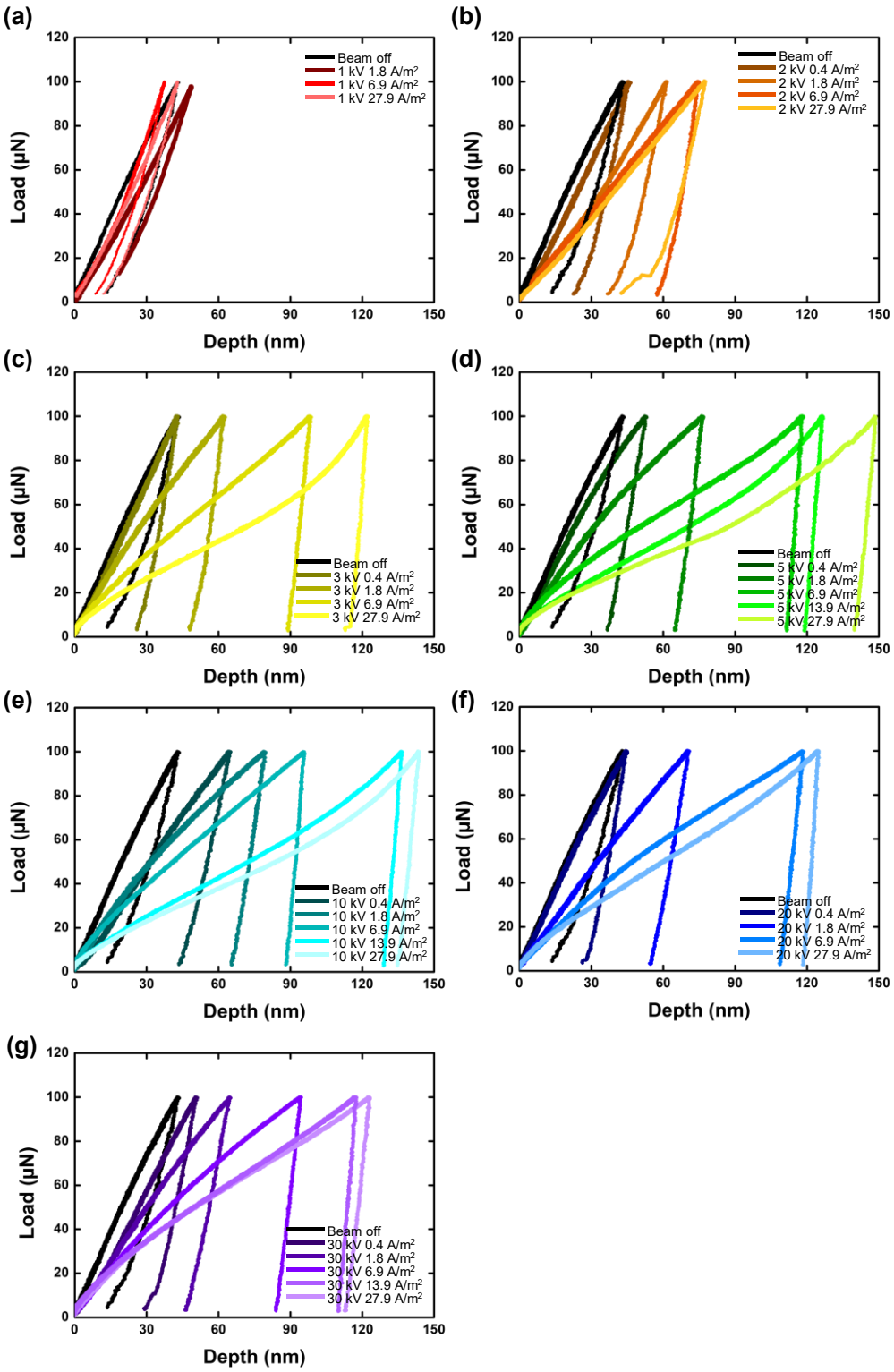

Fig. S10. Compression load-depth curves of the amorphous silica spheres under various e-beam irradiation conditions.

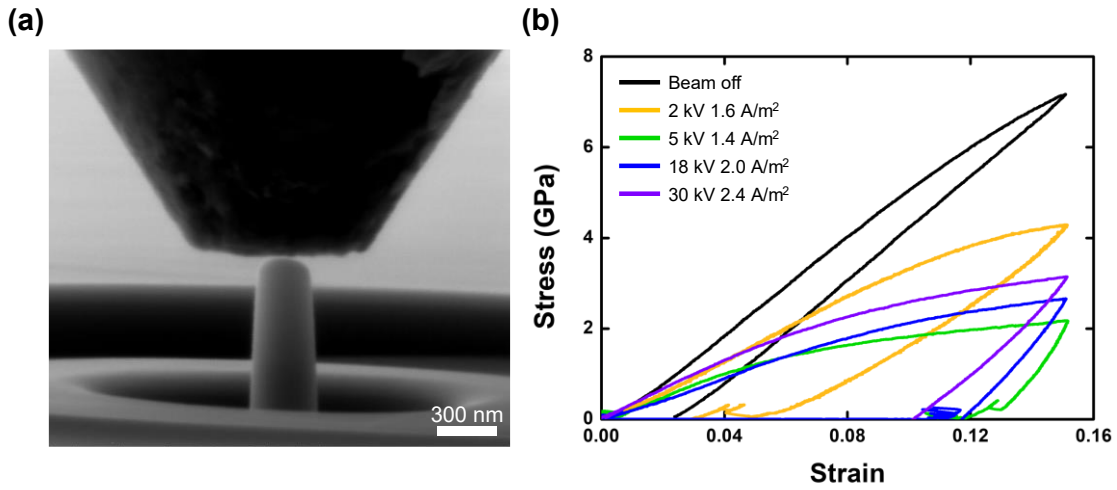

Fig. S11. *In-situ* compression test on the fused quartz pillars using the flat punch indenter. (a) Tilted SEM image of a fused quartz pillar beneath the flat punch indenter prior to the compression test. (b) Engineering stress-strain curves of the fused quartz pillars under various e-beam irradiation conditions.

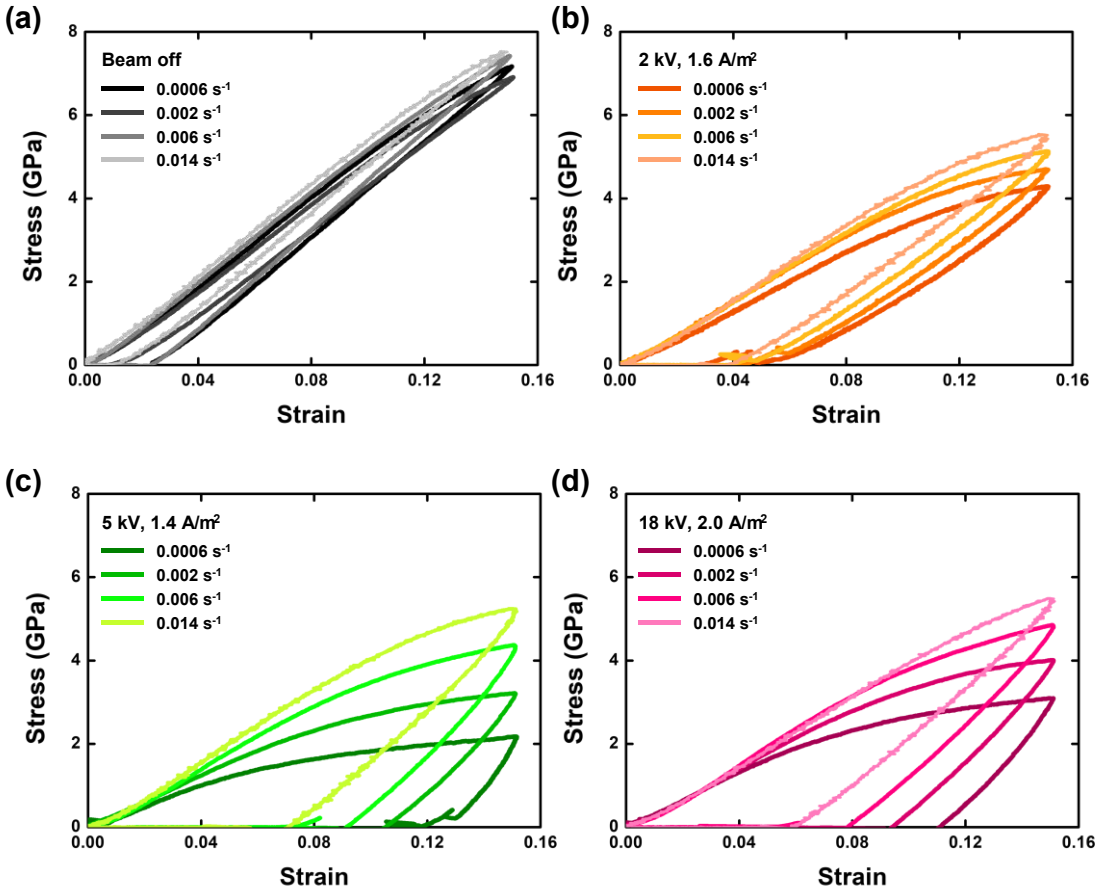

Fig. S12. Engineering stress-strain curves of the fused quartz pillars at various strain rates under (a) beam-off, (b) 2 kV and 1.6 A/m^2, (c) 5 kV and 1.4 A/m^2, and (d) 18 kV and 2.0 A/m^2 e-beam conditions.

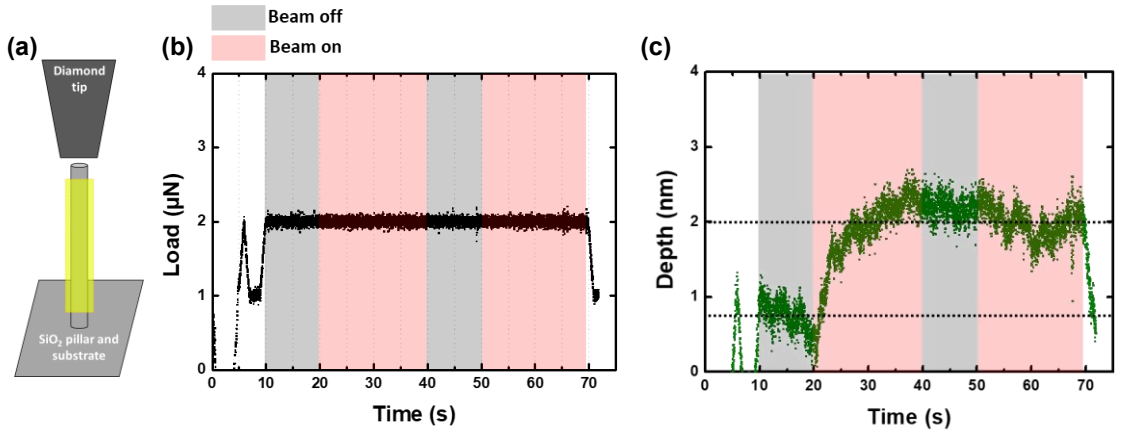

Fig. S13. Temperature change via e-beam irradiation (fused quartz pillar). (a) Schematic diagram of thermal expansion measurement. (b) Loading condition during the measurement. (c) Displacement change during the measurement. Decreasing depth indicates expansion. The viscoplastic deformation of fused quartz occurs at a temperature above the glass transition temperature (Tg) of 1200 °C. If there is a significant temperature rise due to e-beam irradiation, we should observe the thermal expansion of fused quartz. Therefore, we fabricated a fused quartz pillar with a high aspect ratio (diameter of 250 nm and height of 3 μm) and measured the displacement change under e-beam (5 kV and 27.9 A/m^2) irradiation using an *in-situ* nano-indentation system (Hysitron PI-85 SEM PicoIndenter®, Bruker, Billerica, MA, USA) mounted on an SEM stage (FEI Nova 600 NanoLab, Thermo Fisher Scientific, Waltham, MA, USA), as shown in (a). During the measurement, a small load of only 2 μN was applied for stable contact between the indenter and pillar. (b) shows the corresponding loading conditions and time segments for irradiation and no irradiation conditions. If the temperature rises to ~Tg = 1200 °C via e-beam irradiation, the thermal expansion of the fused quartz pillar should be approximately 30 nm. A displacement change as a function of time plot shown in (c) clearly shows that the fused quartz pillar does not expand under e-beam irradiation. Instead, it is compressed by 1.5 nm under e-beam irradiation (first beam-on condition, 20~40 s). After this small compression, there is no displacement change under subsequent beam-off or -on conditions. Therefore, the temperature increase within the fused quartz pillar via e-beam irradiation is almost negligible.

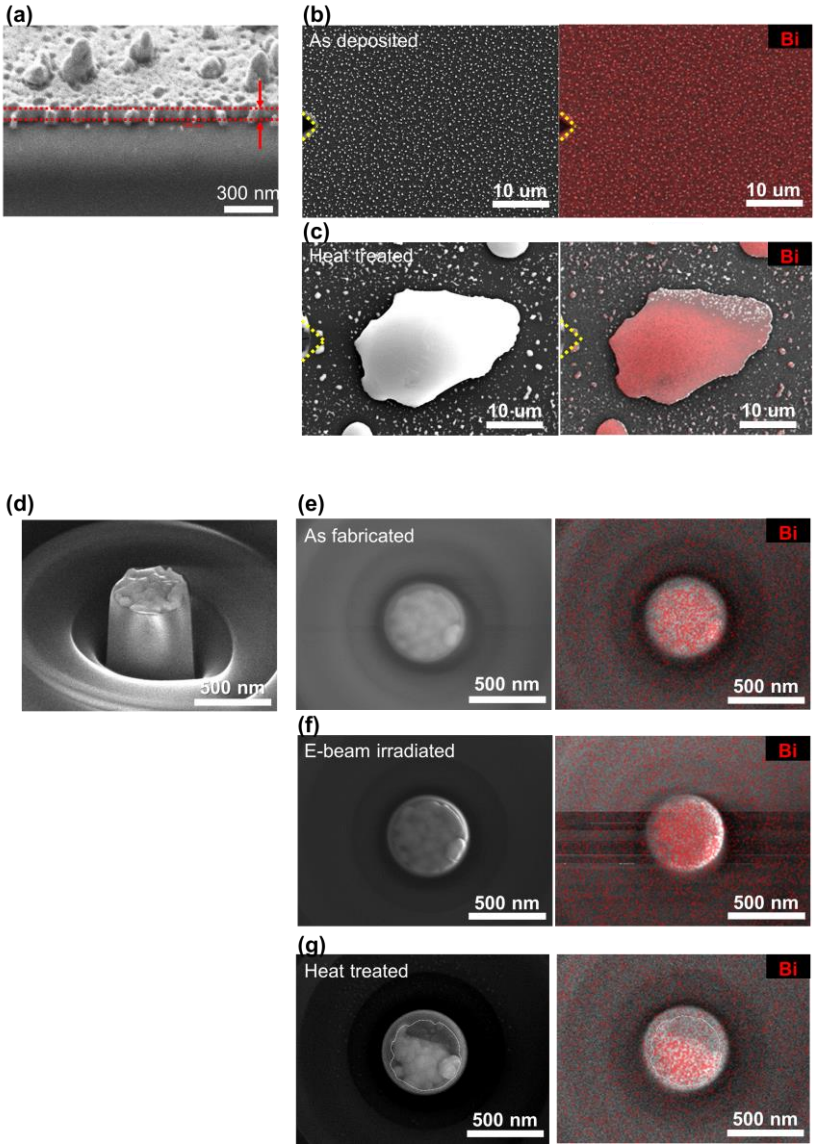

Fig. S14. Temperature change via e-beam irradiation (Bi thin film). (a) Tilted SEM image of the as-deposited Bi film on the fused quartz substrate. Top surface view SEM image (left) and Bi elemental mapping (right) of the Bi film (b) as deposited and (c) heated. (d) Tilted SEM image of the as-fabricated fused quartz pillar with Bi thin film. Top surface view SEM image (left) and Bi elemental mapping (right) of the (e) as fabricated, (f) e-beam irradiated, or (g) heated fused quartz pillar with Bi thin film. To indirectly approximate the temperature increase due to e-beam irradiation within the fused quartz pillar, we evaluated the morphological change in the thin metal film with a low melting temperature deposited on the fused quartz before and after e-beam irradiation. First, we fabricated the fused quartz with a Bi coating, which exhibits a low melting point (271.5 °C). Bi thin film was deposited for 16 min under an RF power of 50 W and working pressure of 40 mtorr, yielding a deposition rate of 6.2 nm/min. The film thickness is approximately 100 nm, as confirmed using by cross-section focused ion beam

(FIB)-SEM (a). Top surface SEM and Bi mapping images (energy dispersive X-ray spectroscopy) shown in (b) reveal that the Bi is deposited on the entire substrate, with fine extrusions. After heating at 450 °C for 20 min, the morphology of the deposited Bi changes significantly. (c) shows the top surface SEM and Bi mapping images, at the same position as that shown in (b), after heating in a vacuum tube furnace at a pressure of $<7.4 \times 10^{-5}$ torr. This is in the range of the typical vacuum condition of SEM. After heating, the Bi coating agglomerates, forming much larger particles (c). Therefore, we fabricated the Bi film + fused quartz pillar system by conducting FIB milling on the fused quartz substrate with deposited Bi and observing the morphological changes in the Bi after e-beam irradiation and heating. (d) show the as-fabricated Bi film + fused quartz pillar. Due to ion beam damage during milling, the deposited Bi exhibits a slightly wrinkled shape. We initially conducted an e-beam irradiation test using SEM (FEI Quanta FEG-250, Thermo Fisher Scientific). The sample was placed on the *in-situ* nano-indentation system (Hysitron PI-85 SEM PicoIndenter®) mounted on the SEM stage to produce the same experimental conditions as the mechanical testing conditions. We conducted e-beam irradiation for 5 min after focusing, at an acceleration voltage and a current density of 5 kV and 42.0 A/m^2, respectively. All other parameters for e-beam irradiation were the same as those used for mechanical testing, except that the indenter was not contacted.

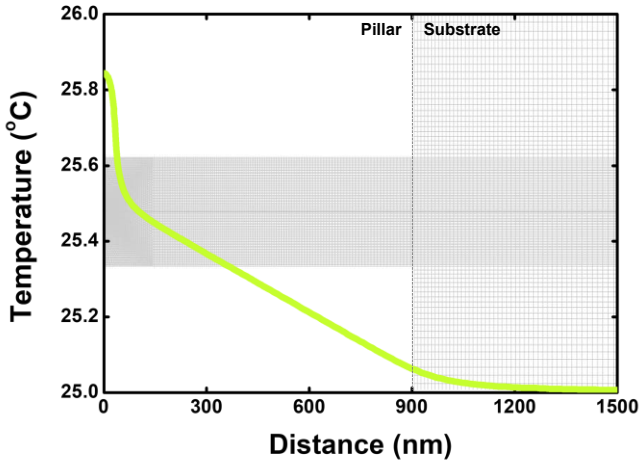

Fig. S15. Temperature change within the fused quartz pillar under a 5 kV, 1.4 A/m^2 e-beam estimated by finite element analysis. The insets show the partial cross-section of the fused quartz pillar and substrate. The temperature rise is < 1 °C. The temperature rise in amorphous silica nanospheres under e-beam irradiation was estimated as follows by assuming that the surface of the nanosphere is at room temperature (RT):

$$k\nabla_{\vec{r}}^2 T = -H$$

where k is the thermal conductivity of amorphous silica and H is the volume heat flux under e-beam irradiation. During the compression tests, the nanosphere (k = 1.46 W/m·K) is in contact with the diamond indenter which has extremely high k (2000 W/m·K), meaning that the surface temperature of the nanosphere is almost at RT. The volume heat flux was obtained from the Monte Carlo simulation. In the case of e-beam with V_A = 3 kV and J = 27.9 A/m^2 which was observed to induce the most prominent super-plastic deformation of amorphous silica in our study, the $\nabla_{\vec{r}}^2 T$ of a nanosphere is -2.12×10^{13} K/m^2. Consistently, the small specimen size results in a temperature rise inside the nanosphere of < 1 °C, suggesting that the thermal activation of ductile plastic deformation is unfavorable. Therefore, it can be deduced that the e-beam athermally induces the ductile plastic deformation of amorphous silica.

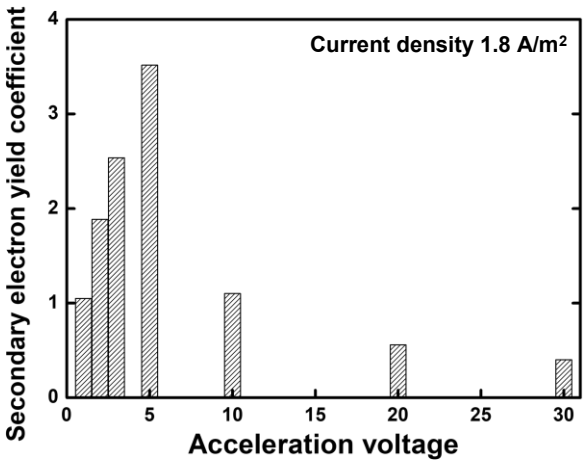

Fig. S16. Secondary electron yield coefficients in the fused quartz pillar under e-beams with varying acceleration voltages and a 1.4 A/m^2 current density calculated via Monte Carlo simulation. Secondary electrons are generated when ionization occurs. We calculated the number of secondary electrons generated within the fused quartz pillar during a single line scan by the SEM e-beam. We set the number of incident electrons to the value corresponding to the current density of 1.8 A/m^2 (Table S2).

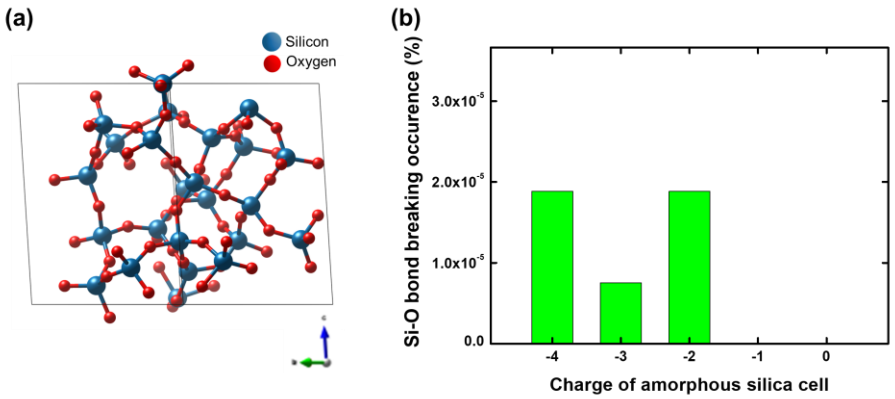

Fig. S17. Density functional theory calculation of bond breaking occurrence in the amorphous silica structures under the e-beam irradiation. (a) One of the amorphous silica structures used for the simulation and (b) Ratio of bond breaking occurrence with respect to the charge of amorphous silica cell. We investigated the number of Si-O bond breaking under compressive stress with and without the e-beam irradiation. To do so, we performed density functional theory calculations with Vienna Ab initio Simulation Package (VASP). Because amorphous SiO_2 structures has no long-range order, first we generate multiple amorphous silica structures to take account of the variation of the amorphous structures. To generate amorphous silica, we carry out first-principles molecular dynamics (FPMD) simulations of SiO_2 melt-quench-annealing process. The initial structures are prepared by randomly distributing 24 Si atoms and 48 O atoms to the cell. The volume of the cell is set to make the density to be 2.65 g/cm^3, which is experimentally known density of amorphous SiO_2. Perdew-Burke-Ernzerhof (PBE) functional is used for the exchange-correlation energy of electrons and the energy cutoff of 500 eV and 2×2×2 k-points mesh is adopted after convergence test. The timestep is set to be 2 fs. Before melting simulations, the randomly generated initial structures are superheated at 4500 K for 20 ps with NVT ensemble to erase initial information of random distribution. From the superheating trajectory, 20 structures are sampled every 1 ps. Subsequently, each sampled structures go through 3000 K melting for 10 ps to get equilibrated liquid structure of SiO_2. After the 10 ps of melting simulation, the structures are cooled to 300 K with 135 K/ps quenching rate. NPT ensemble with 0 external pressure is adopted for melting and quenching simulations. Then, the quenched structures are doped with electrons with 4 different doping levels (undoped and doped with 1, 2, 3, 4). After electron doping, the structures are annealed at 500 K for 4 ps in NPT ensemble to equilibrate atomic positions and cell volume at different doping level. Finally, the atomic positions and cell structures are relaxed at 0 K until the atomic

forces and stress tensors are less then 0.02 eV/Å and 2 kbar, respectively. 100 relaxed structures are used as the amorphous silica samples with different doping levels. For 24×48 Si-O bonds in each sample, we count the number of bond breaking the structures go through under compressive stress and atomic position relaxation.

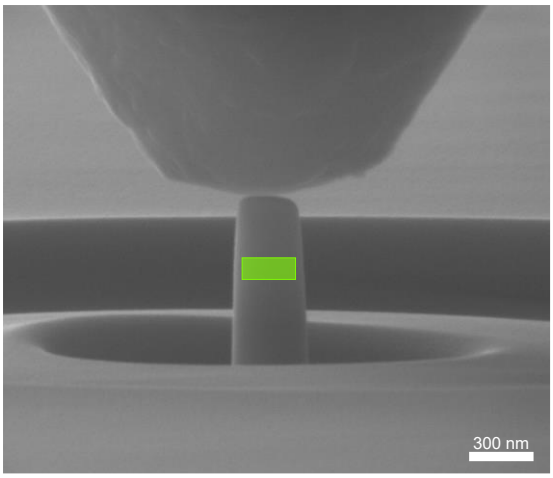

Fig. S18. Mechanical shaping of fused quartz pillars within a selected region. Tilted SEM image of the fused quartz pillar beneath the flat punch indenter prior to the compression test. The green rectangle represents the selected area subjected to e-beam irradiation.

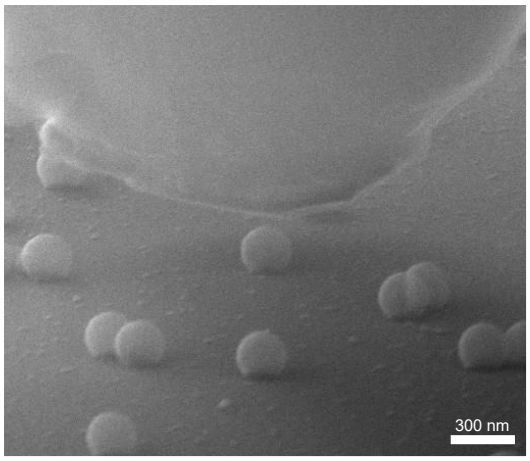

Fig. S19. Mechanical shaping of spherical amorphous silica nanoshell. Tilted SEM image of the fused quartz pillar beneath the cono-spherical indenter prior to the compression test.

Supplementary Tables

Table S1. Experimental parameters of e-beam irradiation.

Acceleration voltage (kV)	Current density (A/m^2)	Magnification	Dwell time (μs)	Number of pixels
1	0.4 / 1.8 / 6.9† / 27.9	× 100,000	1	512 × 442
2	0.4 / 1.6* / 1.8 / 6.9 / 27.9			
3	0.4 / 1.8 / 6.9 / 27.9			
5	0.4 / 1.4* / 1.8 / 6.9 / 13.9 / 27.9 / 913‡			
10	0.4 / 1.8 / 6.9 / 13.9 / 27.9			
18	2.4*			
20	0.4 / 1.8 / 6.9 / 27.9			
30	0.4 / 1.8 / 2.0* / 6.9 / 13.9 / 27.9 / 1606‡			

* e-beam parameters of the compression tests on fused quartz pillars

† e-beam parameters of the mechanical shaping of spherical amorphous silica nanoshells

‡ e-beam parameters of the mechanical shaping of fused quartz pillars

Table S2. Numbers of electrons used in CASINO Monte Carlo simulation.

Current density (A/m^2)	Time of a single horizontal scan of the specimen (μs)	Number of incident electrons during scan	Number of incident electrons in simulation
0.4	100	1,934	2,000
1.8		8,112	8,000*
6.9		31,200	31,000†
13.9		62,400	62,000
27.9		124,800	124,000
Relaxation time (μs)			
913	500	136,840	10,000‡
1606		77,750	

* number of electrons used in the interaction model of a fused quartz pillar

† number of electrons used in the interaction model of the mechanical shaping of spherical amorphous silica nanoshells

‡ number of electrons used in the interaction model of the mechanical shaping of a fused quartz pillar

Supplementary Movies

Movie S1. In-situ compression test of the amorphous silica sphere under a 10-kV, 27.9-A/m2 electron beam.

Movie S2. In-situ compression test of the amorphous silica sphere while alternately turning the 10-kV, 27.9-A/m2 electron beam on and off.